Supplementary Information for

High rate asymmetrical supercapacitor based on Cobalt doped birnessite nanotubes and FeOOH nanotubes

Man Shen[a], Shi Jin Zhu [a,b*], Ziyang Guo[a], Xin Fu[a], Wangchen Huo[a], Chuan Jing[a], Xiaoying Liu[d],, Yu Xin Zhang[a *,c]

[a] *College of Material Science and Engineering, Chongqing University, Chongqing, 400044, P.R. China*

[b] *Institut für Chemie, Technische Universität Chemnitz, Straße der Nationen 62, 09111 Chemnitz, Germany*

[c] *State Key Laboratory of Mechanical Transmissions, College of Materials Science and Engineering, Chongqing University, Chongqing 400044, China*

[d] *Engineering Research Center for Waste Oil Recovery Technology and Equipment, Ministry of Education, College of Environment and Resources, Chongqing Technology and Business University, Chongqing 400067, China*

E-mail: zhangyuxin@cqu.edu.cn; zhushijin1112@gmail.com

Experimental section

Materials

Polycarbonate (PC) membrane was purchased from WHATMAN. Potassium permanganate ($KMnO_4$), cobalt nitrate hexahydrate ($Co(NO_3)_2{\cdot}6H_2O$), N, N-dimethylformamide (DMF) were purchased from Shanghai Aladdin Biochemical Technology Co., Ltd. All reagents were used without any further modification.

Synthesis of the Co^{2+} doped MnO_2 nanotubes

The pure MnO_2 nanotubes and Co doped MnO_2 (Co-MnO_2-X) nanotubes were prepared by a one-step hydrothermal method using a polycarbonate membrane as a template.The polycarbonate (PC) membrane substrates (pore diameter: 200 nm) were treated by the hydrochloric acid (1 M) to remove the impurities on the surface. In a typical synthesis of Co doped samples, 0.11 g $KMnO_4$, and 0.01 g $Co(NO_3)_2{\cdot}6H_2O$ were dissolved in 35 ml deionized water. The molar ratio of cobalt ion to manganese ion is 5%. The treated PC membrane was immersed in the above solution for 10 minutes. The mixture was transferred into a Teflon-lined stainless steel autoclave which was subsequently maintained at 120^{o}C for 6 h. The Co-MnO_2-5/PC membrane composites were then taken out from the solution after reaction time, and then the PC template was dissolved in DMF to obtain pure Co-MnO_2-5 nanotubes. Finally, the Co-MnO_2-5 nanotubes were washed with distilled water and ethanol, and dried at 60^{o}C. The pure MnO_2 nanotubes was prepared in the absence of cobalt nitrate hexahydrate via the above method. Comparatively, Co-MnO_2-3 (Co/Mn atomic ratios of 3%) and Co-MnO_2-10 (Co/Mn atomic ratios of 10%)were prepared with the differern amounts of $Co(NO_3)_2{\cdot}6H_2O$.

Synthesis of the Mn-FeOOH nanotubes

The preparation of Mn-FeOOH nanorods are achieved via a hydrothermal method. Initially, 80 mg $FeSO_4{\cdot}7H_2O$ was dissolved into 32 mL mixed solvent containing distilled water and ethylene glycol (V_D /V_E =7/1) and stirred for about 10 min, respectively. Then, 20 mg Co-MnO_2-5 nanotubes and 32 mL $FeSO_4{\cdot}7H_2O$ mixed solution with were transferred into a 50 mL Teflon-lined stainless steel autoclave and maintained at 120 °C for 2 h. After the reaction, the autoclave was cooled to room temperature. The solid precipitates were washed with distilled water and finally dried at 60°C for 12 h. Because FeOOH nanotubes are prepared with Co-MnO_2-5 nanotubes as a template, a small amount of Mn element will inevitably remain. Due to the residual Mn element, the final sample was Mn-doped FeOOH nanotubes, so we named this sample Mn-FeOOH nanotubes.

Materials characterization

The crystallographic information and chemical compositions of the as-prepared nanostructures were characterized by powder X-ray diffraction (XRD, D/max 2500, Cu Kα). The structures and morphologies of the as-prepared nanostructures were measured by focused ion beam scanning electron microscopy (FIB/SEM, ZEISS AURIGA) and transmission electron microscopy (TEM, FEI Talos F200S G2). XPS spectra were acquired on a Physical Electronics ESCA 5600 spectrometer with a monochromatic Al Kα X-ray source (power: 200 W/14 kV) and a multichannel detector (Omni IV).

Electrochemical measurements

An electrochemical workstation with a three-electrode system was used to test the electrochemical properties of Co-MnO_2-X nanotubes in a 1 M Na_2SO_4 electrolyte. Co-MnO_2-X nanotubes powder as working electrode, platinum plate as counter electrode and the calomel electrode as reference electrode. The working electrode was prepared by mixing an active material, carbon black, and polyvinylidenefluoride (PVDF) which dissolved in N-methyl-2-pyrrolidone (NMP) with a mass ratio of 7:2:1, and then uniformly coating the above slurry on the foamed nickel. The electrode was kept at 120^{o}C for 12 h under 10 MPa. The positive electrode materials were studied by cyclic voltammetry (CV), galvanostatic charge-discharge (CC), and electrochemical impedance spectroscopy (EIS). The CV curves at different scan rates of 10-100 mV S^{-1} were tested at a potential window of 0-0.8 V. CC curves were measured with current densities ranged from 1 to 10 A g^{-1} in the potential of 0 to 0.8 V. The electrochemical impedance spectroscopy (EIS) was conducted in the frequency range between 100 kHz and 0.01 Hz with a perturbation amplitude of 5 mV versus the open-circuit potential. The electrochemical properties of FeOOH nanotubes was measured by the same way, but the potential window is -1.0-0.

The asymmetric supercapacitor was measured with a two-electrode system using two slices of the electrode material of the same size, a piece of Whatman filter paper as the separator, and two pieces of nickel foil as the current collectors. In the two-electrode system, the Co-MnO_2 nanotubes were used as the positive electrode materials and the Mn-FeOOH nanotubes was used as nagative electrode materals

Calculation equations

1 Single Electrode

The specific capacitance (C_m) of the electrode was calculated from their charge-discharge curves by the following equations

$$C_m = \frac{I\Delta T}{m\Delta V}$$

where m, I, ΔT and ΔV are the weight (g) of the electroactive materials, discharge current (A), the discharging time (s), and the discharging potential range (V), respectively.

2 ASC device

The total capacitance (C), was calculated from their charge-discharge curves according to the following equation

$$C = \frac{I\Delta T}{M\Delta V}$$

where I, ΔT and ΔV is discharge current (A), the discharging time (s), and the discharging potential range (V), respectively, M is the sum of the masses of MnO_2 and AG.

Energy density (E) and average power density (P) was calculated by the following equations

$$E = \frac{0.5C\Delta V^2}{3.6}$$

$$P = \frac{E}{\Delta t}$$

Δt (s) is discharge time, I (A) is discharge current, and ΔV is voltage window.

Theoretical calculations

The Gaussian smearing width was set to 0.2 eV. The Brillouin zone was sampled with a 3 × 6 × 2 K points. All atoms were converged to 0.01 eV $Å^{-1}$. A plane-wave basis fulfil cut-off energy of 500 eV, which was employed within the framework of the projector-augmented wave method. A 2 × 2 ×2 supercell of bulk MnO_2 that includes 99 atoms was first relaxed, after optimization, cobalt atoms are intercalated between layers and replaced with manganese atoms.

The energy required to insert cobalt between the manganese dioxide layers (ΔE_i) is defined as:

$$\Delta E_i = E_{Co\text{-}in} - E_{MnO2} - E_{Co} \quad (1)$$

The energy required for cobalt to replace manganese (ΔE_r) is defined as:

$$\Delta E_r = E_{Co\text{-}Mn} - E_{MnO2} - E_{Co} + E_{Mn} \quad (2)$$

Where $E_{Co\text{-}in}$, $E_{Co\text{-}Mn}$, E_{MnO2}, E_{Co}, E_{Mn} depict the energy of cobalt intercalated MnO_2, cobalt replaced manganese MnO_2, pure MnO_2, Co, Mn.

Supplementary Figures

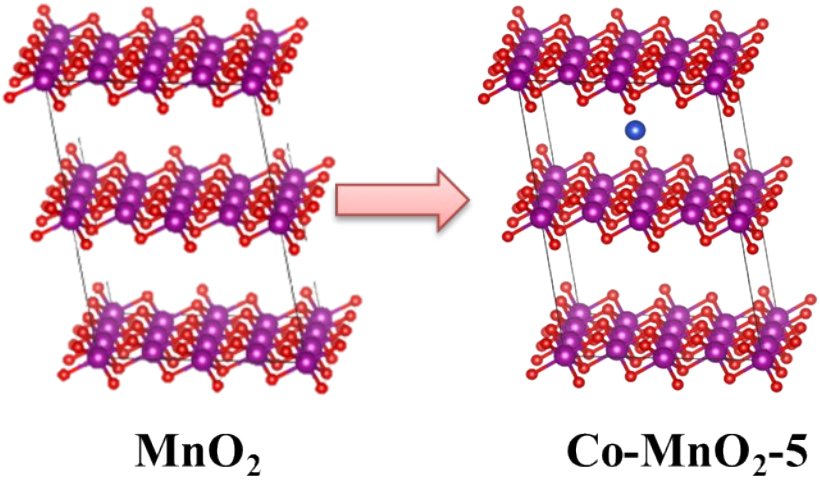

Fig. S1 Crystal structure of MnO_2 and Co-MnO_2-5

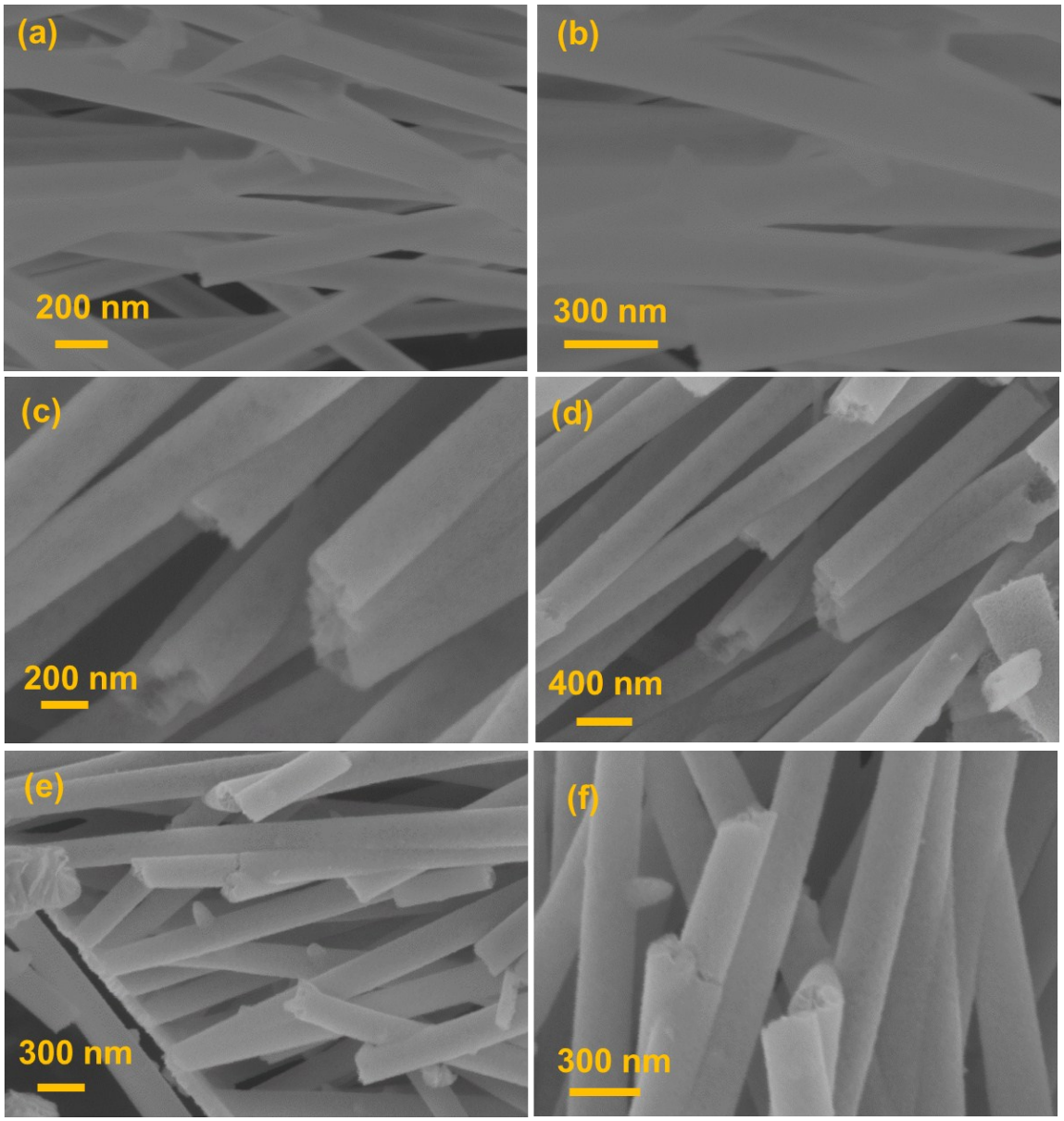

Fig. S2 **(a)-(b)** SEM images of MnO_2, **(c)-(d)**SEM images of Co-MnO_2-3, **(d)-(e)** SEM images of Co-MnO_2-10.

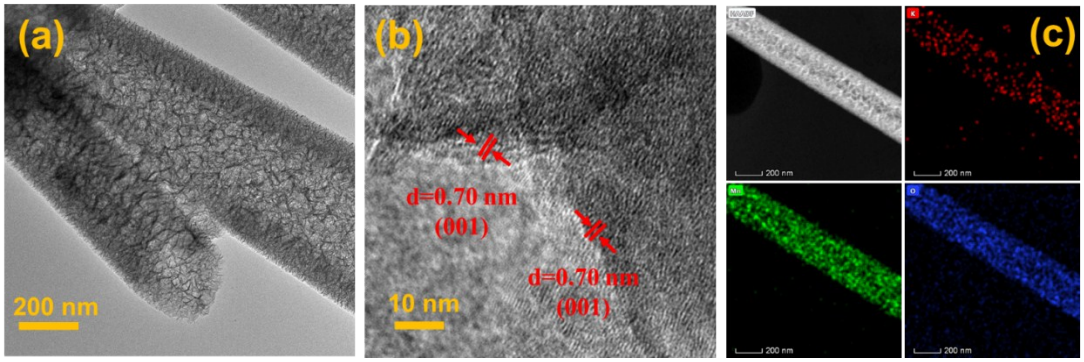

Fig. S3 TEM, HRTEM, TEM-EDS mapping images of MnO_2 nanotubes.

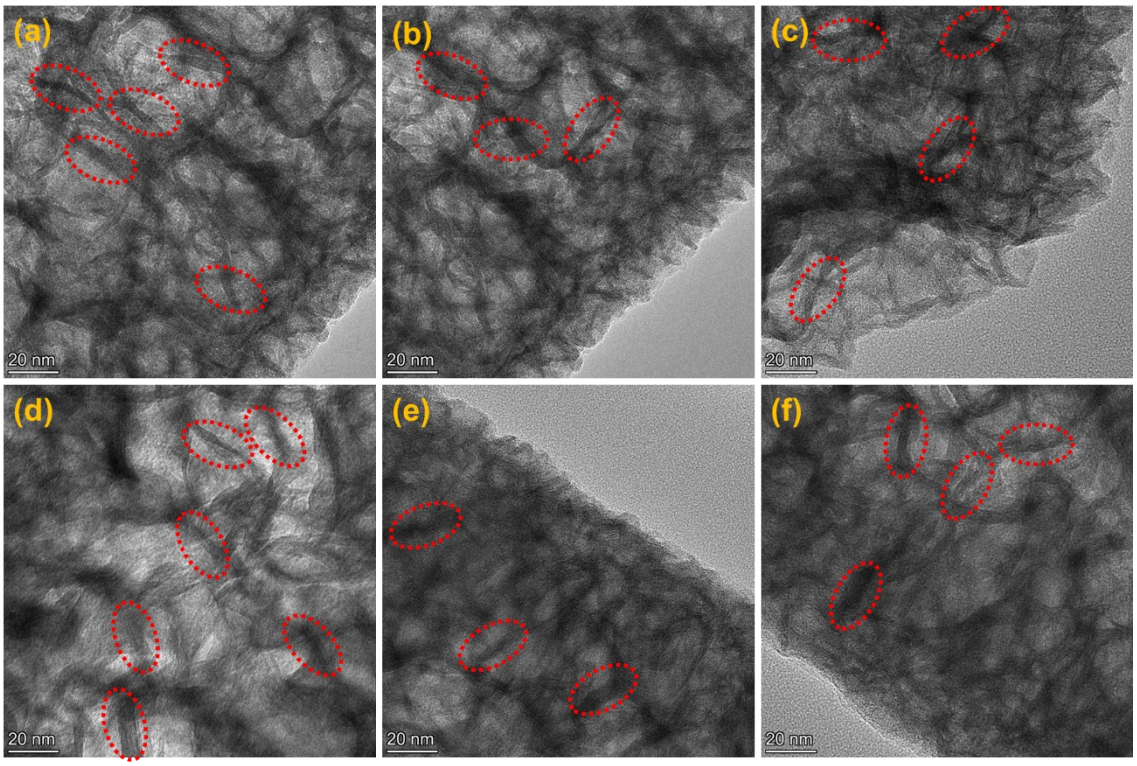

Fig. S4 HETEM images: **(a)-(c)** MnO_2 nanotubes; **(d)-(f)** Co-MnO_2-5 nanotubes.

These high-resolution transmission electron microscopy images fully show that MnO_2 nanotubes and Co-MnO_2-5 nanotubes are composed of extremely thin nanosheets. The positions marked by the red circles in Fig. S4 is the cross section of the nanosheets, and the width of the cross section of the nanosheets represents the thickness of the nanosheets. In the HRTEM images of each sample, more than 20 nanoflake sections were taken, their cross-section widths were measured, and then their average and variance were calculated. Finally we get that the nanosheets of MnO_2 nanotubes are in the range of 3.57 ∓ 0.761 nm, and the thickness of nanosheets of Co-MnO_2-5 nanotubes are in the range of 3.99 ∓ 1.07 nm.

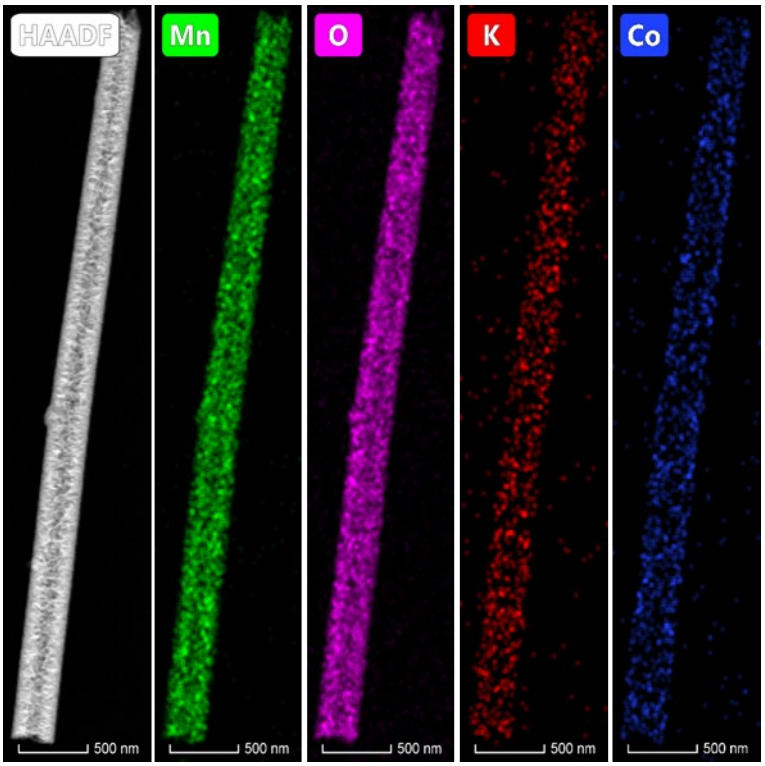

Fig. S5 TEM-EDS mapping image of Co-MnO_2-5 nanotubes.

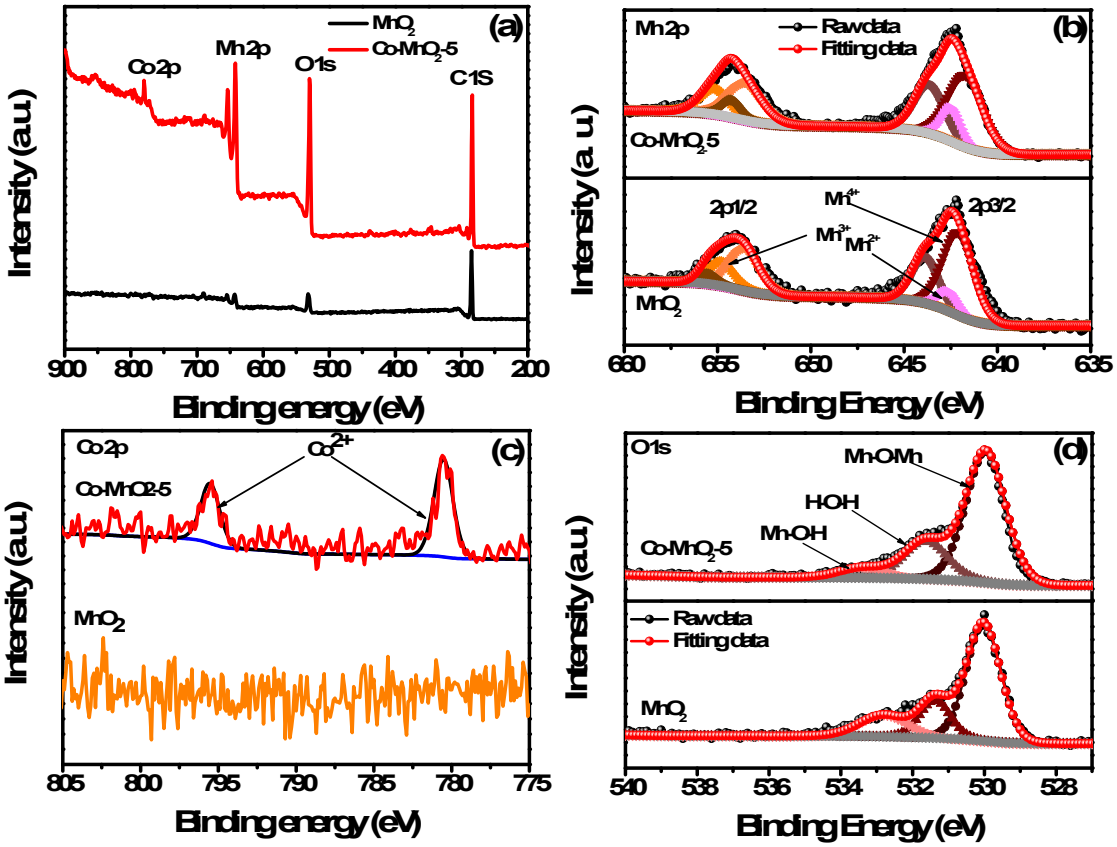

Fig S6 XPS patterns of Co-MnO_2-5 and MnO_2. **(a)** XPS survey spectrum. High-resolution spectra of **(b)** Mn 2p, **(c)** Co2p, and **(d)** O1s.

The XPS analysis in Fig. S6a (survey spectra) reveals that Co-MnO_2-5 with an apparent Co 2p peaks, indicating cobalt exists in the two-dimensional layered structure of MnO_2. As illustrated in the Fig. S6b, there is no significant difference in the high-resolution XPS spectra of the Mn 2p regions of MnO_2 and Co-MnO_2-5 nanotubes, both of which contain two main peaks, which leads to spin orbit doublet of Mn $2p_{3/2}$ and Mn $2p_{1/2}$ peaks. The binding energy of the two peaks of the two samples was approximately 642.3 and 653.9 eV, and the spin energy separation was 11.6 eV, which means that the valence of the Mn element was about +4. The two spin orbits of MnO_2 nanotubes are divided into three peaks (Mn^{4+}, Mn^{3+}, Mn^{2+}). For 2p1/2, the corresponding binding energies are 653.6eV, 654.8eV, 655.5eV, and for 2p3/2, the corresponding binding energies are 642.1eV. 643.8eV, 642.6eV. Similarly, the two spin orbits of Co-MnO_2-5 nanotubes are also divided into three peaks representing different valence states. The three peaks of 2p1/2 are located at 653.5eV, 655.1eV, 654.3eV, that is 641.7eV, 643.6eV, 642.5eV for 2p3/2. To evaluate the contribution of Mn^{4+}, Mn^{3+}, Mn^{2+}, the relative proportion was decided by the ratio of peak area. As for MnO_2 nanotubes, the molar ratio of $Mn^{4+}/Mn^{3+}/Mn^{2+}$ was 1.52:0.74:0.23. and the molar ratio of $Mn^{4+}/Mn^{3+}/Mn^{2+}$ for Co-MnO_2-5 nanotubes is 1.52:1.03:0.70. We can see that the proportion of Mn^{4+} ions decreased when doped with cobalt, mainly because a small amount of Mn^{4+} ions were reduced. Similarly, the Co spectrum of Co-MnO_2-5 in Figure S6c shows a doublet at 780.5 and 795.5 eV corresponding to Co^{2+} with a spin-energy separation of 15.0 eV, indicating the successful doping of Co^{2+} ions into MnO_2. In the O 1s core level spectra, three peaks can be clearly identified for the two samples (Fig. S6d), which represent metal oxides (Mn-O-Mn, Co-O-Co), hydrated

metal oxides(Mn-O-H, Co-O-H), and residual water(H-O-H), with corresponding binding energies around 530.0 eV, 531.7 eV, and 533.4 eV, respectively.

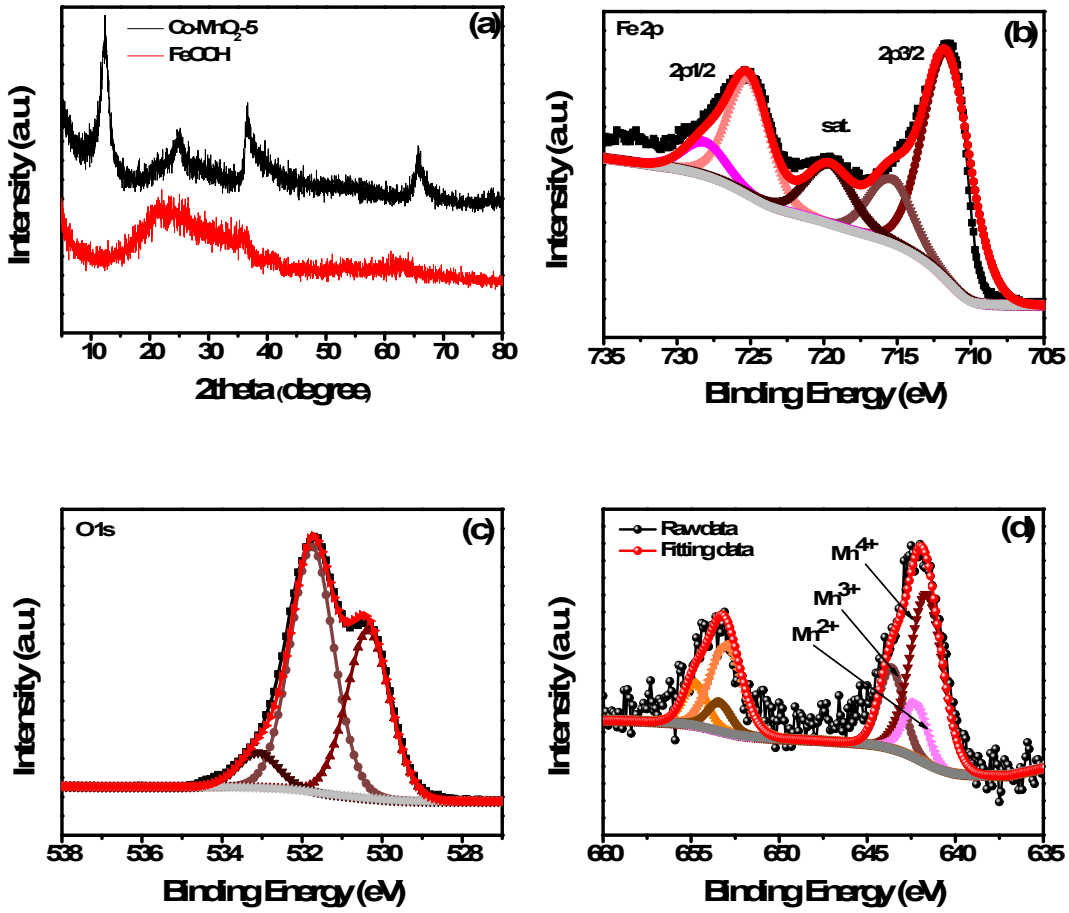

Fig. S7 **(a)** XRD patterns of Co-MnO_2 nanotubes and Mn-FeOOH nanotubes. XPS patterns of FeOOH nanotubes: **(b)** Fe 2p; **(c)** O 1s; **(d)** Mn 2p

.

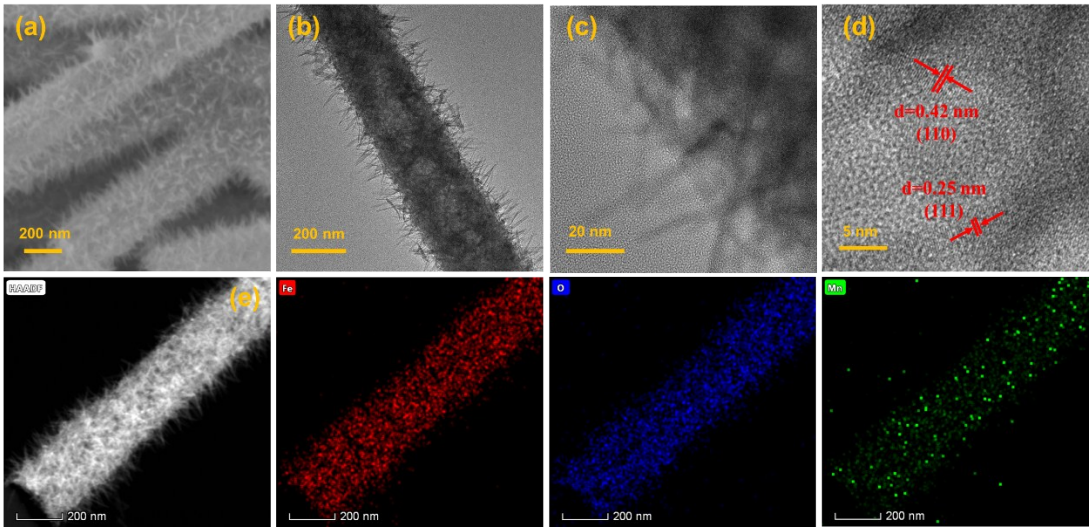

Fig.S8**(a)** SEM image of FeOOH nanotubes, **(b)** TEM image of FeOOH nanotubes, **(c)-(d)** HRTEM image of FeOOH nanotubes, **(d)** TEM-EDS mapping image of Mn-FeOOH nanotubes.

High-energy-density supercapacitors need a negative electrode material with superior performance. Iron oxides/hydroxides are considered to be superior anode materials for supercapacitor. Mn-FeOOH nanotubes prepared by a sacrificial template method. XRD patterns of Co-MnO_2-5 nanotubes and Mn-FeOOH nanotubes are shown in Fig. S7a, which displays that the peak belonging to δ-MnO_2 completely disappears after the transformation. The pronounced peaks centered at 21.2°, 36.6°, 61.7° could be index to the (110), (111), (002) planes of goethite Mn-FeOOH (JCPDS No. 81-0463, a= 4.616Å), respectively. The chemical composition and electronic structure of the and FeOOH nanotubes were investigated by X-ray photoelectron spectroscopy (XPS) and the results are in good agreement with the XRD results. Fig. S7b showed the Fe 2p spectrum of Mn-FeOOH. The spectrum are consist of the peaks of Fe2p3/2 and Fe 2p1/2 with one shakeup satellites (719.6 eV), which are divided into Fe^{2+} and Fe^{3+} peaks at binding energy of 715.4 eV and 711.6 eV for Fe 2p3/2 and 728.1 and 725.1 eV for Fe 2p1/2. The molar ratio of Fe^{2+}/Fe^{3+} is 0.43:1.52. Fig. S7c is the O 1s spectrum of Mn-FeOOH nanotubes, which is decomposed into three peaks corresponding to M-O-H (531.7 eV), M-O-M (530.3 eV) and H-O-H (533.1 eV) bonding. M stands for Fe and Mn. Unlike MnO_2, the peak area of M-O-H is the largest in the O 1s spectrum of Mn-FeOOH, which indicates the presence of -OH groups. Fig.S7d shows that the Mn element exists in Mn-FeOOH nanotubes, but because the amount is relatively small, the noise of the Mn2p spectrum is relatively large. Similar to MnO_2, we can also see the existence of three valence states of Mn in the Mn2p spectrum of Mn-FeOOH, but Mn^{4+} is the majority. Fig. S8a displays the representative SEM image of Mn-FeOOH nanotubes. Unlike Co-MnO_2-5 nanotubes, Mn-FeOOH nanotubes are composed of many nanorods, which indicates that the MnO_2 nanosheets gradually transformed into FeOOH nanorods during the hydrothermal process. The transformation of δ-MnO_2 with two-dimensional layered structure into α-FeOOH with 1x1 tunnel structure leads to the transformation of morphology[1-3]. Simultaneously, the diameter of Mn-FeOOH nanotubes is in the range of 350-450 nm, which is larger than that of Co-MnO_2-5 nanotubes. More details of Mn-FeOOH nanotubes are shown in the TEM and HRTEM images (Fig.S8b-d). The fine Mn-FeOOH nanorods with the average diameter of about 8 nm the average length of about 45 nm. HETEM image, corresponding to (110) and (111) planes of goethite FeOOH. TEM-EDS mapping image is demonstrated in Fig. S8e, shows that Fe element and O element evenly distribute on the Mn-FeOOH nanotubes. But at the same time, we also see a small amount of Mn element uniformly distributed in Mn-FeOOH nanotubes. Combining the results shown in

Fig.S7d and Fig.S8e shows that after the transformation, a small amount of Mn element remains.

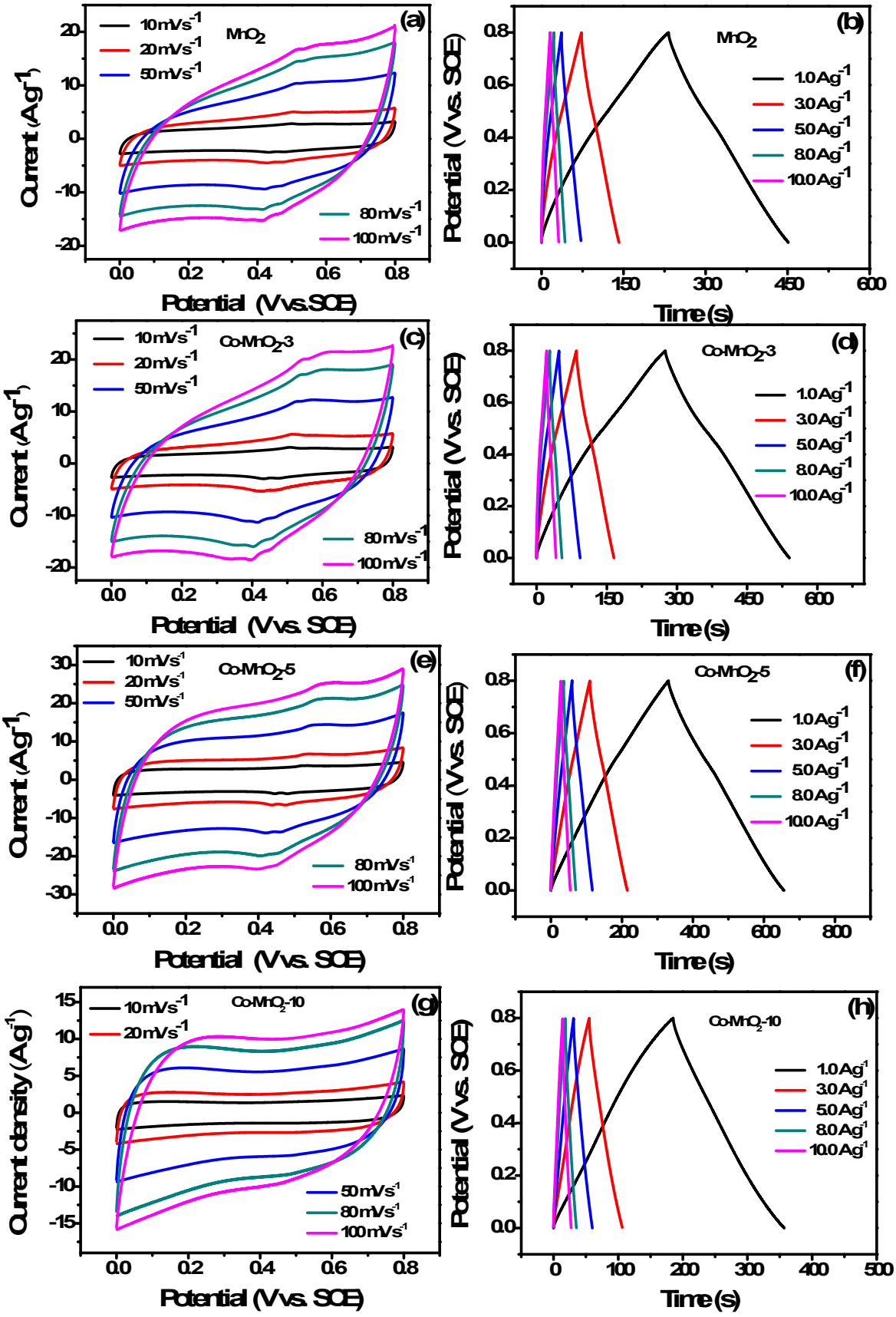

Fig S9 CV curves at different scan rates and CC curves at different current densities. **(a)-(b)** MnO_2, **(c)-(d)** Co-MnO_2-3, **(e)-(f)** Co-MnO_2-5, **(g)-(h)** Co-MnO_2-10.

Table S1 Specific capacitance of the MnO_2, Co-MnO_2-3, Co-MnO_2-5, Co-MnO_2-10 nanotubes electrodes under different current densities.

Samples	***1* (A g^{-1})**	***3* (A g^{-1})**	***5* (A g^{-1})**	***8* (A g^{-1})**	***10*A g^{-1})**
MnO_2	273.8	257.3	222.5	205.0	195.0
Co-MnO_2-3	331.4	300.8	281.9	261.0	248.8
Co-MnO_2-5	406.4	395.6	358.8	341.0	331.3
Co-MnO_2-10	215.0	192.6	181.3	170.0	163.8

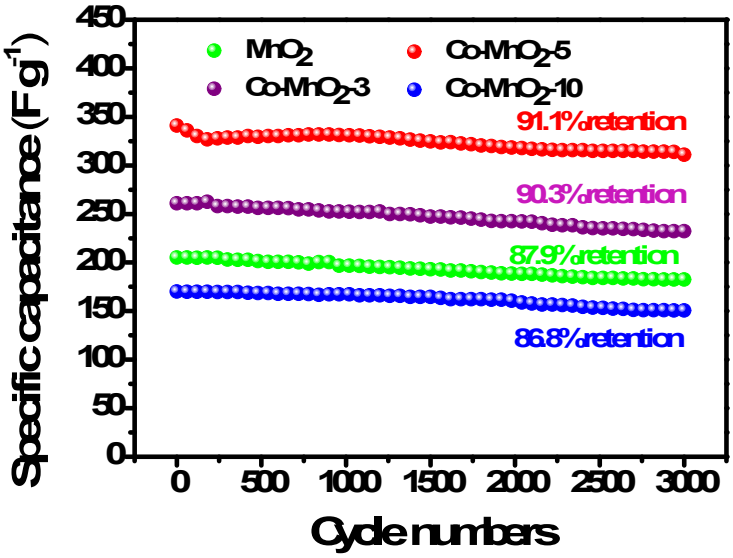

Fig. S10 Cycling performance of MnO_2 , Co-MnO_2-3, Co-MnO_2-5, Co-MnO_2-10 electrodes at the current density of 8 A g^{-1}.

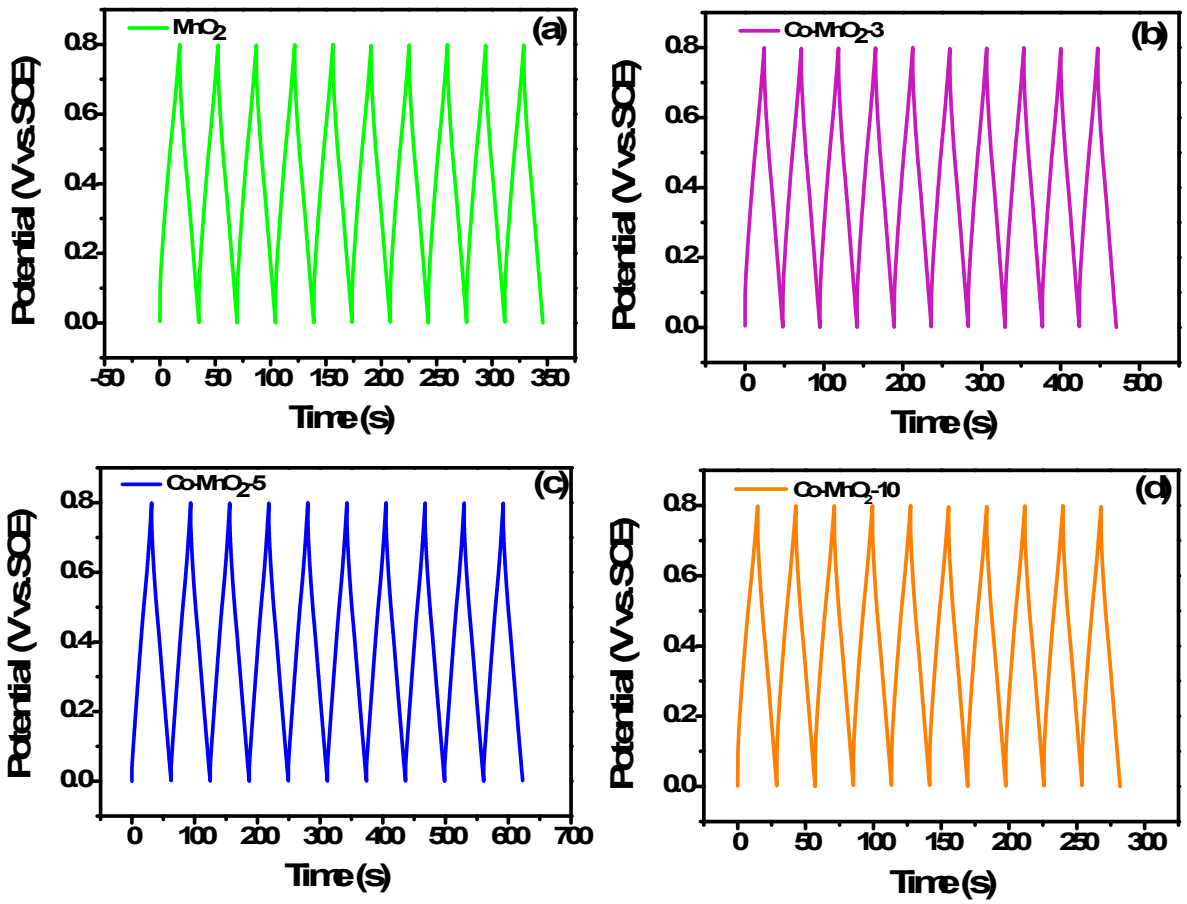

Fig. S11 CC curves for the last ten cycles of all samples. **(a)** MnO_2, (**b**) Co-MnO_2-3, (**c**) Co-MnO_2-5, (**d**) Co-MnO_2-10.

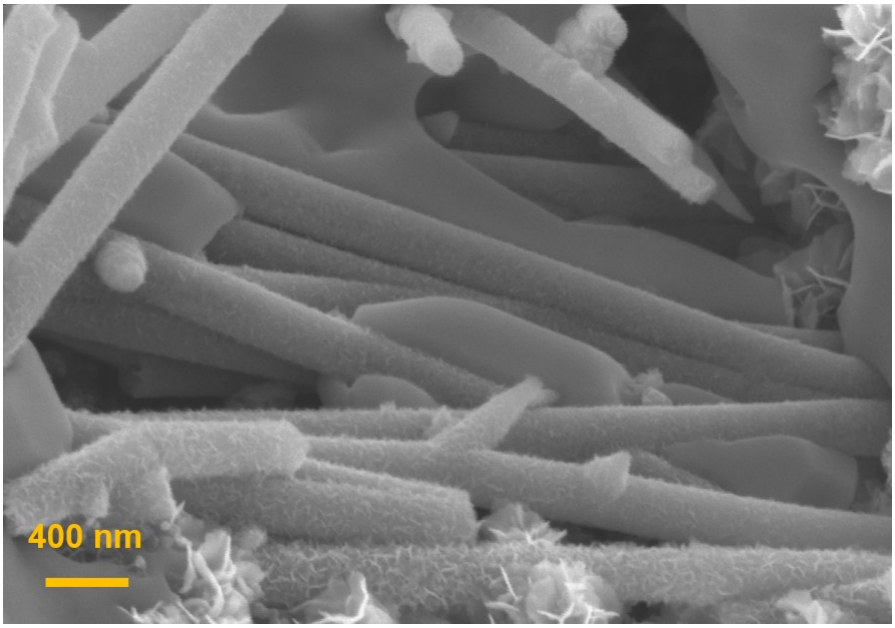

Fig. S12 The corresponding SEM image of the Co-MnO_2-5 electrode after 3000 electrochemical cycles.

Table S2 Comparison of specific capacitances of the reported (last five years) MnO_2 electrodes and the present work. All values are measured using the three-electrode system.

Samples	*Cs* (F g^{-1})	Electrolyte	Test condition	References
Amorphous hierarchical porous MnO_2	391.9	1 M Na_2SO_4	0.1 A g^{-1}	4
MnO_2/HCS-30	255	1 M Na_2SO_4	1 A g^{-1}	5
α-MnO_2@δ-MnO_2 nanostructures	206	1 M Na_2SO_4	0.25 A g^{-1}	6
3DHG/MnO_2	192.2	1 M Na_2SO_4	0.5 A g^{-1}	7
MnO_2/GNF-0.5	201	1 M Na_2SO_4	1 A g^{-1}	8
Fe_3O_4@MnO_2 nanospheres	243.7	1 M KOH	0.1 A g^{-1}	9
MnO_2/3D CNTs-G/Cu	365	1 M Na_2SO_4	1 A g^{-1}	10
Sn-doped MnO_2	243.6	1 M Na_2SO_4	1 A g^{-1}	11
MnO_2/RGO	333.9	1 M Na_2SO_4	0.5 A g^{-1}	12
N-CNTs/MnO_2-2	366.5	0.5M Li_2SO_4	0.5 A g^{-1}	13
MnO_2-ENGP	368.3	1 M Na_2SO_4	0.2 A g^{-1}	14
MnO_2/FAFSC	202.5	1 M Na_2SO_4	10 mV s^{-1}	15
MnO_2/rEGO	342.8	6 M KOH	0.5 A g^{-1}	16
Hierarchical hollow MnO_2 nanofiber	291	1 M Na_2SO_4	1 A g^{-1}	17
Hierarchical multidimensional MnO_2	311.5	1 M Na_2SO_4	0.3 A g^{-1}	18
CSN-PB/MnO_2	315.3	1 M Na_2SO_4	1 A g^{-1}	19
δ-MnO_2/NRGO	299.5	1 M Na_2SO_4	5 mV s^{-1}	20
MnO_2/Ppy	290	0.1M $Ca(NO_3)_2{\cdot}4H_2O$	0.5 A g^{-1}	21
MnO_2 film	369	0.5 M Na_2SO_4	1 A g^{-1}	22
MnO_2/PBC	139.6	1 M Na_2SO_4	0.3 A g^{-1}	23
MnO_2/g-C_3N_4@PPy	274	1 M Na_2SO_4	2 A g^{-1}	24
Fe doped δ-MnO_2	158	1 M Na_2SO_4	0.5A g^{-1}	25
MnO_2/HCNFs	293.6	1 M Na_2SO_4	0.5 A g^{-1}	26
HNPC/MnO_2	204.6	2M Ca $(NO_3)_2$	1 A g^{-1}	27
g-C_3N_4/MnO_2	174	1 M Na_2SO_4	5 mV s^{-1}	28
MnO_2/rGO	255	1 M Na_2SO_4	0.5 A g^{-1}	29
MnO_2@MoS_2	352	2 M KOH	1 A g^{-1}	30
G@MnO_2	245	1 M Na_2SO_4	0.5 A g^{-1}	31
bowl-like MnO_2 nanosheets	379	1 M Na_2SO_4	0.5 A g^{-1}	32
Al-doped MnO_2 nanowires	101	1 M Na_2SO_4	200 mV s^{-1}	33
CNC-MnO_2	306.3	PVA/KOH	0.5 A g^{-1}	34
MnO_2/rGO	234.8	1 M Na_2SO_4	0.1 A g^{-1}	35
porous MnO_2	253	1 M Na_2SO_4	0.5 A g^{-1}	36
δ-MnO_2 hollow microspheres	216.4	1 M Na_2SO_4	0.5 A g^{-1}	37

Cu-MOF@δ-MnO_2 nanosheets	340	1 M Na_2SO_4	1 A g^{-1}	[38]
hollow carbon nanosphere/MnO_2	292.5	1 M Na_2SO_4	1 A g^{-1}	[39]
Sodium-Doped MnO_2	154	0.5 M $Na2_SO_4$	25 mV s^{-1}	[40]
α-MnO_2 nanotube	173	1 M Na_2SO_4	1 A g^{-1}	[41]
Birnessite-type MnO_2	140	1 M Na_2SO_4	1 A g^{-1}	[42]
Birnessite-type MnO_2 nanoflowers	197	1 M Na_2SO_4	1 A g^{-1}	[43]
Fe-doped MnO_2	267	1 M Na_2SO_4	0.1 A g^{-1}	[44]
MnO_2 nanobelts	235	1 M Na_2SO_4	25 mV s^{-1}	[45]
MnO_2 spheres	200	0.65 M K_2SO_4	2 mV s^{-1}	[46]
α-MnO_2 nanorods	198	1 M Na_2SO_4	1 A g^{-1}	[47]
Single-layer MnO_2 nanosheets	163	LiCl/PVA	5 A g^{-1}	[48]
β-MnO_2@δ-MnO_2	200	1 M LiOH	0.05 A g^{-1}	[49]
Nest-like hollow MnO_2	211	1 M Na_2SO_4	1 A g^{-1}	[50]
α-MnO_2 nanowires@ ultrathin δ-MnO_2 nanosheets	230.7	6 M KOH	1 A g^{-1}	[51]
2D δ-MnO_2 nanosheets	306	1 M Na_2SO_4	0.2 A g^{-1}	[52]
Cauliflower−like δ−MnO_2	202	1 M Na_2SO_4	5 mV s^{-1}	[53]
Co-MnO_2-5 nanotubes	**406.4**	**1 M Na_2SO_4**	**1 A g^{-1}**	**This work**

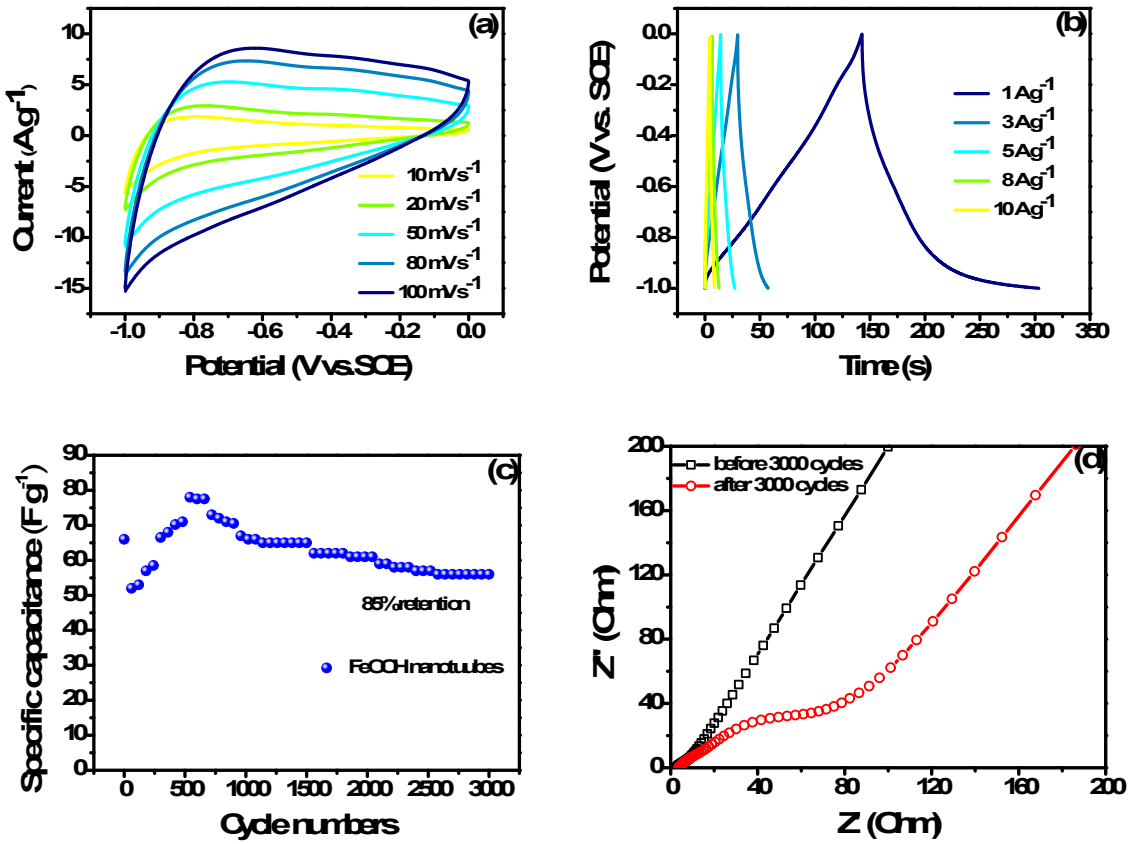

Fig. S13 **(a)** Cyclic voltammograms of Mn-FeOOH electrodes in a 1 M Na_2SO_4 aqueous electrolyte. **(b)** Charge-discharge curves of AG electrodes at different current densities. **(c)** Cycling performance of AG electrodes at the current density of 3 A g^{-1}. **(d)** Electrochemical impedance spectrum of Mn-FeOOH electrodes at open circuit potential in the frequency range from 0.01 Hz to 100 kHz.

The CV curves of the Mn-FeOOH nanotubes electrode at different scan rates of 10-100 mV s^{-1} exhibit a semirectangular shape that is an indicative of pseudocapacitive behavior. The pseudocapacitance of Mn-FeOOH nanotubes might arise from a reversible Fe^{3+}/Fe^{2+} couple, while the identity of the charge cations involved in the redox reaction was yet undetermined. Typical galvanostatic charge/discharge curves of Mn-FeOOH electrode collected at different current densities are shown in Fig. S13b. The specific capacitances of Mn-FeOOH nanotubes electrode achieves 162.4, 91.8, 69.3, 56.3 and 50.2 F g-1 at current density of 1, 3, 5, 8 and 10 A g^{-1}, respectively. Moreover, a further cycling test to Mn-FeOOH nanotubes electrode is shown in Fig. S13c. It is obvious that the Mn-FeOOH nanotubes electrode has 85.0% capacitance retention after 3000 cycles. Fig. S13d shows its EIS plots of the first cycle and the last cycle and suggested that the performance of the electrode material changed a little more, which indicated that Mn-FeOOH nanotubes electrode owned a relatively good cycling stability. On the other hand, the electrochemical performance of Mn-doped FeOOH nanotubes is superior to that

of pure α-FeOOH nanotubes(Mn-FeOOH nanotubes)[2].

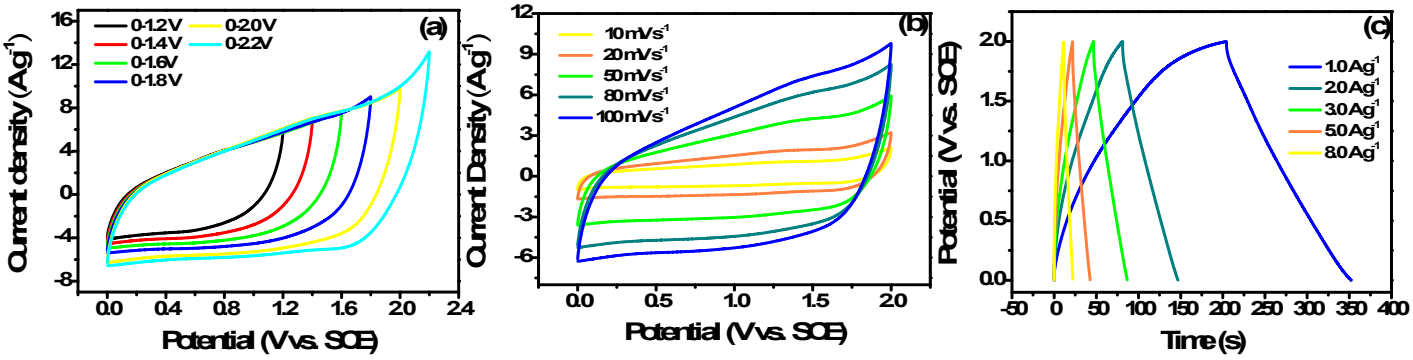

Fig. S14 **(a)** CV curves of Co-MnO_2-5// Mn-FeOOH with different potentials, **(b)** CV curves of Co-MnO_2-5// Mn-FeOOH with different scan rates, **(c)** CC curves of Co-MnO_2-5// Mn-FeOOH with different current densitie

Table S3 The capacitive properties of the containing-MnO_2 supercapacitors.

Capacitor	Energy density (Wh kg^{-1})	Reference
Hollow nanostructured MnO_2//AC	7.2	[54]
Fe-MnO_2 //AC	20.2	[55]
δ-MnO_2 //δ-MnO_2	8.2	[37]
CNT/CNF/MnO_2// CNT/CNF/MnO_2	3.8	[56]
MnO_2/$MnCO_3$/rGO//rGO	17.8	[57]
MnO_2/AC//AC	24.6	[58]
MnO_2-CNT //AC	25	[59]
MnO_2 //AC	18.2	[60]
MnO_2/ carbon nanocoil// carbon nanocoil	21.58	[61]
K_xMnO_2@CNF//ACNF	21.1	[62]
CNTf-MnO_2-60// CNTf-MnO_2-60	21	[63]
3D graphene/α-MnO_2 NWs// 3D graphene	38	[64]
MnO_2/Ti_3C_2// MnO_2/Ti_3C_2	8.3	[65]
CC@T-Nb_2O_5@MnO_2//GO	31.76	[66]
3D-MnO_2//AC	36.6	[67]
Ni-Mn LDH@MnO_2//AC	16	[68]
MnO_2// Fe_2O_3	22.8	[69]
MnO_2// RGO	22.2	[70]
MnO_2/La_2O_3//AC	25.8	[71]
MnO_2/rGO// MnO_2/rGO	24	[72]
$MnCO_3$@MnO_2//AG	27.4	[73]
Co-MnO_2-5 nanotubes // Mn-FeOOH nanotubes	42.1	This work

References

1 F. Lin, M. Yuan, Y. Chen, Y. Huang, J. Lian, J. Qiu, H. Xu, H. Li, S. Yuan, Y. Zhao and S. Cao, *Electrochim. Acta*, 2019, **320**, 134580.

2 L. B. Zhong, Q. Liu, J. Q. Zhu, Y. S. Yang, J. Weng, P. Wu and Y. M. Zheng, *ACS Sustainable Chemistry & Engineering*, 2018, **6**, 2991-3001.

3 D. Zhang, X. Kong, M. Jiang, D. Lei and X. Lei, *ACS Sustainable Chemistry & Engineering*, 2019, **7**, 4420-4428.

4 Q. Ma, M. Yang, X. Xia, H. Chen, L. Yang and H. Liu, *Electrochim. Acta*, 2018, **291**, 9-17.

5 W. Du, X. Wang, J. Zhan, X. Sun, L. Kang, F. Jiang, X. Zhang, Q. Shao, M. Dong, H. Liu, V. Murugadoss and Z. Guo, *Electrochim. Acta*, 2019, **296**, 907-915.

6 Y. Guo, L. Li, L. Song, M. Wu, Y. Gao, J. Chen, C. Mao, J. Song and H. Niu, *J. Mater. Chem. A*, 2019, **7**, 12661-12668.

7 Y. Chai, Z. Li, J. Wang, Z. Mo and S. Yang, *Journal of Alloys and Compounds*, 2019, **775**, 1206-1212.

8 X. Lv, H. Zhang, F. Wang, Z. Hu, Y. Zhang, L. Zhang, R. Xie and J. Ji, *CrystEngComm*, 2018, **20**, 1690-1697.

9 J. Ding, J. Yang, S. Ji, S. Huo and H. Wang, *Ionics*, 2018, **25**, 665-673.

10 T. Bi, H. Fang, J. Jiang, X. He, X. Zhen, H. Yang, Z. Wei and Z. Jia, *Journal of Alloys and Compounds*, 2019, **787**, 759-766.

11 B. Lan, S. Huang, C. Ye, Q. Qin, J. Yan and Y. Wu, *Journal of Alloys and Compounds*, 2019, **788**, 302-310.

12 S. Sun, G. Jiang, Y. Liu, B. Yu and U. Evariste, *Journal of Electronic Materials*, 2018, **47**, 5993-5999.

13 J. Zhu, X. youlong, J. Hu, L. Wei, J. Liu and M. Zheng, *J. Power Sources*, 2018, **393**, 135-144.

14 X. Feng, Y. Li, G. Chen, Z. Liu, X. Ning, A. Hu, Q. Tang and X. Chen, *Materials Letters*, 2018, **231**, 114-118.

15 A. A. Mohammed, C. Chen and Z. Zhu, *J. Power Sources*, 2019, **417**, 1-13.

16 H. Wang, Q. Fu and C. Pan, *Electrochim. Acta*, 2019, **312**, 11-21.

17 K. Xu, S. Li, J. Yang and J. Hu, *Journal of colloid and interface science*, 2018, **513**, 448-454.

18 X. Bai, X. Tong, Y. Gao, W. Zhu, C. Fu, J. Ma, T. Tan, C. Wang, Y. Luo and H. Sun, *Electrochim. Acta*, 2018, **281**, 525-533.

19 G. Zhang, H. Yao, F. Zhang, Z. Gao, Q. Li, Y. Yang and X. Lu, *Nano Research*, 2019, **12**, 1061-1069.

20 J. Q. Liu, W. Zhao, G. L. Wen, J. Xu, X. Chen, Q. Zhang, Y. Wang, Y. Zhang and Y. C. Wu, *Journal of Alloys and Compounds*, 2019, **787**, 309-317.

21 S. Shivakumara and N. Munichandraiah, *Journal of Alloys and Compounds*, 2019, **787**, 1044-1050.

22 J. Liu, L. Yang, Z. Song and C. Xu, *Applied Surface Science*, 2019, **478**, 94-102.

23 G. Yang and S.-J. Park, *Journal of Alloys and Compounds*, 2018, **741**, 360-367.

24 S. Sun, L. Guo, X. Chang, Y. Yu and X. Zhai, *Materials Letters*, 2019, **236**, 558-561.

25 L. Yan, L. Niu, C. Shen, Z. Zhang, J. Lin, F. Shen, Y. Gong, C. Li, X. Liu and S. Xu, *Electrochim. Acta*, 2019, **306**, 529-540.

26 P. Zhao, M. Yao, H. Ren, N. Wang and S. Komarneni, *Applied Surface Science*, 2019, **463**, 931-938.
27 L. Sun, N. Li, S. Zhang, X. Yu, C. Liu, Y. Zhou, S. Han, W. Wang and Z. Wang, *Journal of Alloys and Compounds*, 2019, **789**, 910-918.
28 J. Kavil, P. M. Anjana, P. Periyat and R. B. Rakhi, *Sustainable Energy & Fuels*, 2018, **2**, 2244-2251.
29 Q. Zhang, X. Wu, Q. Zhang, F. Yang, H. Dong, J. Sui and L. Dong, *Journal of Electroanalytical Chemistry*, 2019, **837**, 108-115.
30 N. Kanaujiya, N. Kumar, A. K. Srivastava, Y. Sharma and G. D. Varma, *Journal of Electroanalytical Chemistry*, 2018, **824**, 226-237.
31 L. Wang, Y. Ouyang, X. Jiao, X. Xia, W. Lei and Q. Hao, *Chemical Engineering Journal*, 2018, **334**, 1-9.
32 P. Liu, Y. Zhu, X. Gao, Y. Huang, Y. Wang, S. Qin and Y. Zhang, *Chemical Engineering Journal*, 2018, **350**, 79-88.
33 Y. Zeng, *International Journal of Electrochemical Science*, 2019, DOI: 10.20964/2019.05.64, 4350-4360.
34 L. M. Chen, H. Y. Yu, D. C. Wang, T. Yang, J. M. Yao and K. C. Tam, *ACS Sustainable Chemistry & Engineering*, 2019, **7**, 11823-11831.
35 Y. Chen, J. Zhang, M. Li, C. Yang, L. Zhang, C. Wang and H. Lu, *Electrochim. Acta*, 2018, **292**, 115-124.
36 G. Zhang, L. Ren, D. Hu, H. Gu and S. Zhang, *Journal of colloid and interface science*, 2018, **518**, 84-91.
37 W. Xiao, W. Zhou, H. Yu, Y. Pu, Y. Zhang and C. Hu, *Electrochim. Acta*, 2018, **264**, 1-11.
38 J. Xu, Y. Wang, S. Cao, J. Zhang, G. Zhang, H. Xue, Q. Xu and H. Pang, *J. Mater. Chem. A*, 2018, **6**, 17329-17336.
39 J. Dong, G. Lu, J. Yue, Z. Cheng and X. Kang, *Applied Surface Science*, 2019, **480**, 1116-1125.
40 T. M. Ou, C. T. Hsu and C. C. Hu, *Journal of The Electrochemical Society*, 2015, **162**, A5124-A5132.
41 C. Wang, F. Li, Y. Wang, H. Qu, X. Yi, Y. Lu, Y. Qiu, Z. Zou, B. Yu and Y. Luo, *Journal of Alloys and Compounds*, 2015, **634**, 12-18.
42 X. Zhang, W. Miao, C. Li, X. Sun, K. Wang and Y. Ma, *Materials Research Bulletin*, 2015, **71**, 111-115.
43 S. Zhao, T. Liu, D. Hou, W. Zeng, B. Miao, S. Hussain, X. Peng and M. S. Javed, *Applied Surface Science*, 2015, **356**, 259-265.
44 Z. Wang, F. Wang, Y. Li, J. Hu, Y. Lu and M. Xu, *Nanoscale*, 2016, **8**, 7309-7317.
45 M. Aghazadeh, M. G. Maragheh, M. R. Ganjali, P. Norouzi and F. Faridbod, *Applied Surface Science*, 2016, **364**, 141-147.
46 A. Gambou-Bosca and D. Bélanger, *Electrochimica Acta*, 2016, **201**, 20-29.
47 W. He, W. Yang, C. Wang, X. Deng, B. Liu and X. Xu, *Physical chemistry chemical physics : PCCP*, 2016, **18**, 15235-15243.
48 Y. Yu, Y. Zhai, H. Liu and L. Li, *Materials Letters*, 2016, **176**, 33-37.
49 Q. Liu, J. Yang, R. Wang, H. Wang and S. Ji, *RSC Advances*, 2017, **7**, 33635-33641.
50 B. Ke, J. Wang, D. Li, S. Zhao, L. Luo, L. Yu and S. Hussain, *Journal of Materials Science: Materials in Electronics*, 2016, **28**, 418-425.
51 Z. Ma, G. Shao, Y. Fan, G. Wang, J. Song and D. Shen, *ACS Appl. Mater. Interfaces*, 2016, **8**, 9050-9058.

52 P. Gao, P. Metz, T. Hey, Y. Gong, D. Liu, D. D. Edwards, J. Y. Howe, R. Huang and S. T. Misture, *Nature Comm.*, 2017, **8**, 14559.
53 P. R. S. Fitri Nur Indah Sari , Jyh-Ming Ting, *Journal of American Ceramic Society*, 2017, DOI: 10.1111/jace.14636, 11.
54 L. Gao, L. Zhang, S. Jia, X. Liu, Y. Wang and S. Xing, *Electrochim. Acta*, 2016, **203**, 59-65.
55 A. G. Zhongchun Li , Zhengsong Lou , Jianhua Sun , Quanfa Zhou , and Kwong Yu Chan , *Journal of materials science*, 2017, **52**, 14.
56 T. Wang, D. Song, H. Zhao, J. Chen, C. Zhao, L. Chen, W. Chen, J. Zhou and E. Xie, *J. Power Sources*, 2015, **274**, 709-717.
57 Y. Liu, D. He, H. Wu, J. Duan and Y. Zhang, *Electrochim. Acta*, 2015, **164**, 154-162.
58 B. Zhou, Y. Sui, J. Qi, Y. He, Q. Meng, F. Wei, Y. Ren and X. Zhang, *Journal of Electronic Materials*, 2019, **48**, 3026-3035.
59 F. Ochai-Ejeh, M. J. Madito, K. Makgopa, M. N. Rantho, O. Olaniyan and N. Manyala, *Electrochim. Acta*, 2018, **289**, 363-375.
60 C. C. H. Tran, J. Santos-Peña and C. Damas, *The Journal of Physical Chemistry C*, 2017, **122**, 16-29.
61 S. Shi, G. Wan, L. Wu, Z. He, K. Wang, Y. Tang, X. Xu and G. Wang, *Journal of Colloid and Interface Science*, 2019, **537**, 142-150.
62 S. C. Lin, Y.T. Lu, J. A. Wang, C. C. M. Ma and C. C. Hu, *J Power Sources*, 2018, **400**, 415-425.
63 A. Pendashteh, E. Senokos, J. Palma, M. Anderson, J. J. Vilatela and R. Marcilla, *J. Power Sources*, 2017, **372**, 64-73.
64 T. S. Tran, K. M. Tripathi, B. N. Kim, I.-K. You, B. J. Park, Y. H. Han and T. Kim, *Materials Research Bulletin*, 2017, **96**, 395-404.
65 W. Liu, Z. Wang, Y. Su, Q. Li, Z. Zhao and F. Geng, *Advanced Energy Materials*, 2017, **7**, 1602834.
66 T. Wang, Q. Le, J. Zhang, Y. Zhang and W. Li, *Electrochim. Acta*, 2017, **253**, 311-318.
67 Y. Li, Z. Xu, D. Wang, J. Zhao and H. Zhang, *Electrochim. Acta*, 2017, **251**, 344-354.
68 W. Quan, C. Jiang, S. Wang, Y. Li, Z. Zhang, Z. Tang and F. Favier, *Electrochim. Acta*, 2017, **247**, 1072-1079.
69 L. Feng, G. Li, S. Zhang and Y. X. Zhang, *Ceramics International*, 2017, **43**, 8321-8328.
70 S. Shivakumara and N. Munichandraiah, *Solid State Communications*, 2017, **260**, 34-39.
71 Y. Li, B. Guan, A. Maclennan, Y. Hu, D. Li, J. Zhao, Y. Wang and H. Zhang, *Electrochim. Acta*, 2017, **241**, 395-405.
72 E. Miniach, A. Śliwak, A. Moyseowicz, L. Fernández-Garcia, Z. González, M. Granda, R. Menendez and G. Gryglewicz, *Electrochim. Acta*, 2017, **240**, 53-62.
73 H. Chen, Z. Yan, X. Y. Liu, X. L. Guo, Y. X. Zhang and Z.-H. Liu, *J. Power Sources*, 2017, **353**, 202-209.